Supporting Information

Oxygen-vacancy-mediated electron localization at the nickel sites in nickel/iron layered double hydroxide towards efficient oxygen evolution reaction

Jing Zhang,[a,b] Meng Li,[c] Zhiqiang Qiao,[a,b] Kaixuan Huo,[d] Yang Yang,[e] Deqiang Ji,[a,b] Dandan Yuan,[a,b] Liyu Lin,[f*] Zhida Li,[a,b,e*] Hongjun Wu[a,b*]

a National Key Laboratory of Continental Shale Oil, Northeast Petroleum University, Daqing, Heilongjiang 163318, China

b College of New Energy and Materials, Northeast Petroleum University, Daqing, Heilongjiang 163318, China

c College of New Energy, State Key Laboratory of Heavy Oil Processing, China University of Petroleum (East China), Qingdao 266580, China.

d College of Chemistry and Chemical Engineering, State Key Laboratory of Heavy Oil Processing, China University of Petroleum (East China), Qingdao 266580, China.

e State Key Laboratory of Urban Water Resource and Environment, School of Civil and Environmental Engineering, Harbin Institute of Technology, Shenzhen 518055, China

f College of New Materials and New Energies, Shenzhen Technology University, Shenzhen, 518118, China

Corresponding author: Zhida Li (lizhida@hit.edu.cn), Liyu Lin (linliyu@sztu.edu.cn), Hongjun Wu (hjwu@nepu.edu.cn)

1 Experimental Details

1.1 Chemicals

All chemicals utilized in this study were procured from Aladdin and employed as received without any additional purification. The deionized water (DI H_2O) employed in the experimental procedures was generated using an ultrapure purification system (Edi-S0UVF).

1.2 Synthetic procedures

1.2.1. Cleaning of the nickel foam (NF) substrate

The synthesis of NiFe-LDH was carried out using a conventional electrodeposition technique in a standard three-electrode setup. Prior to the electrodeposition process, a nickel foam (NF) substrate measuring 1 cm × 2 cm was meticulously cleaned using a series of sequential steps. First, it was subjected to acetone, followed by immersion in a 2 M HCl solution, and subsequently rinsed with ethanol and deionized water (DI H_2O) using bath sonication for 15 minutes for each solvent. This cleaning procedure effectively eliminated the surface NiO layer. Subsequently, the cleaned NF substrate was dried in a vacuum oven at a temperature of 40 °C overnight to ensure complete removal of any residual moisture.

1.2.2 NiFe-LDH synthesis process

The synthetic procedures can be found in the main article.

1.2.3. RuO_2 electrode preparation

The comparison sample of RuO_2 was loaded onto NF via a drop-casting method. Specifically, 10 mg of commercial RuO_2 powder was dispersed in a solution containing 195 μL of ethanol, 775 μL of DI H_2O, and 30 μL of Nafion solution. The dispersion was subjected to bath sonication for 30 minutes to ensure homogeneity. Subsequently, 50 μL of the RuO_2 suspension was drop-casted onto a 1 cm × 2 cm NF substrate. The RuO_2/NF was then dried in a vacuum oven at 40 °C for approximately 4 hours to remove any residual solvents and ensure the stability of the RuO_2 coating.

1.3 Characterization of catalysts

Microscopic morphological features of the NiFe-LDH samples were investigated using Scanning Electron Microscopy (SEM) and Transmission Electron Microscopy (TEM) techniques. The SEM analysis was performed using a SIGM instrument from Zeiss Company, while the TEM analysis was conducted using an FEI-TALOS-F200X microscope. Energy dispersive X-ray (EDX) data were acquired using the Super-X system. Inductively coupled plasma optical emission spectrometry (ICP-OES) analysis was conducted using a Thermo Fisher iCAP 7400 spectrometer. The crystal structure and phase composition were characterized by X-ray Diffraction (XRD) using a Bruker D8 Advance instrument. To explore the electronic structure, X-ray Photoelectron Spectroscopy (XPS) measurements were carried out using a Thermofisher Escalab 250xi spectrometer. The XPS spectra obtained were analyzed using XPS peak software to determine the elemental compositions and valence states. The binding energy was calibrated using the C 1s peak at 284.6 eV. Raman spectra were acquired using the HORIBA JY LabRAM HR Evolution device with an Ar-ion laser operating at 532 nm.

Electron Paramagnetic Resonance (EPR) measurements were performed using a Bruker EMX spectrometer operating in the X-band frequency range. The X-ray absorption spectra (XAS) including X-ray absorption near-edge structure (XANES) and extended X-ray absorption fine structure (EXAFS) of the sample at Ni-edge was collected at the Beamline of TPS44A1 in National Synchrotron Radiation Research Center (NSRRC), Taiwan. 3.0 GeV a pair of channel-cut Si (111) crystals was used in the monochromator.

1.4 Electrochemical measurements

Electrochemical measurements were performed using a CHI 660E electrochemistry workstation in a 1M KOH electrolyte at room temperature. A typical three-electrode configuration was employed, with a Pt foil serving as the counter electrode and a Hg/HgO electrode as the reference electrode. All potentials in this study were converted to the reversible hydrogen electrode (RHE) scale according to: $E_{RHE} = E_{apply} + 0.0592 * pH + 0.098\ V$. The overpotential ($\eta$) of the OER was calculated using the equation: $\eta = E_{RHE} - 1.23$.

Prior to the regular electrochemical tests, continuous cyclic voltammetry (CV) scans were performed until a stable and reproducible CV curve was obtained. Polarization curves, also known as Linear Sweep Voltammograms (LSV), were recorded at a scan rate of 5 mV s^{-1} with 90% iR compensation. Electrochemical Impedance Spectroscopy (EIS) measurements were carried out at an overpotential of 230 mV over a frequency range of 10^5 to 0.1 Hz. The electrochemical active surface area (ECSA) was evaluated by calculating the electrochemical double-layer capacitances (C_{dl}) based on the CV results. CV measurements were conducted with varying scan rates of 20, 40, 60, 80,

and 100 mV s^{-1} within the potential range of 1.024 to 1.124 V vs RHE. Stability assessment was performed through continuous CV running (2000 cycles) and chronoamperometric measurements.

1.5 Density of Functional Theory (DFT) Calculations

In this work, Vienna ab initio simulation package (VASP)[1, 2] was employed to perform DFT calculations within the generalized gradient approximation (GGA) according to the Perdew-Burke-Ernzerhof (PBE)[3] formulation. The projected augmented wave (PAW) potentials were chosen to describe the ionic cores. Valence electrons were taken into account by a plane wave basis set with a kinetic energy cutoff of 400 eV. The electronic energy was considered self-consistent when the energy change was smaller than 10^{-4} eV; a geometry optimization was thought to be convergent when the energy change was smaller than 0.03 eV Å^{-1}. The Brillourin zone was sampled with a gamma-centered grid $2 \times 2 \times 1$ for all computational process. Considering the strong d-electron correlation effects for Fe and Ni, DFT + U method was used in this work with U =3.9 eV and J = 0 eV for Fe and U = 2.9 eV and J = 0 eV for Ni.[4]

The OER process usually summarized in four steps:

$$*+H_2O \rightarrow {}^*OH+H^+ +e^- \qquad \Delta G_{\mathrm{I}} \qquad (1)$$

$$^*OH \rightarrow {}^*O+H^+ +e^- \qquad \Delta G_{\mathrm{II}} \qquad (2)$$

$$*+H_2O \rightarrow {}^*OOH + H^+ + e^- \quad \Delta G_{\mathrm{III}} \qquad (3)$$

$$^*OOH \rightarrow O_2+H^+ +e^- +* \qquad \Delta G_{\mathrm{IV}} \qquad (4)$$
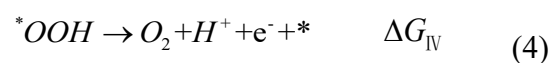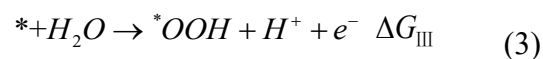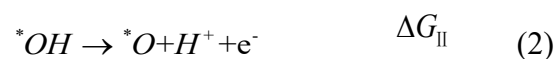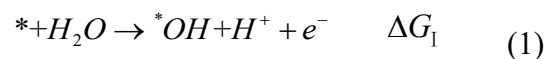
here * denotes adsorption active site on the substrate.

$$\Delta G_{\mathrm{I}} = \Delta G_{*_{OH}} \tag{5}$$

$$\Delta G_{\mathrm{II}} = \Delta G_{*_{O}} - \Delta G_{*_{OH}} \tag{6}$$

$$\Delta G_{\mathrm{III}} = \Delta G_{*_{OOH}} - \Delta G_{*_{O}} \tag{7}$$

$$\Delta G_{\mathrm{IV}} = 4.92 - \Delta G_{*_{OOH}} \tag{8}$$

The overpotential (η) is defined as below:

$$\eta = \max \{\Delta G_{\mathrm{I}}, \Delta G_{\mathrm{II}}, \Delta G_{\mathrm{III}}, \Delta G_{\mathrm{IV}}\} - 1.23\mathrm{e}V \tag{9}$$

2 Supplementary Figures
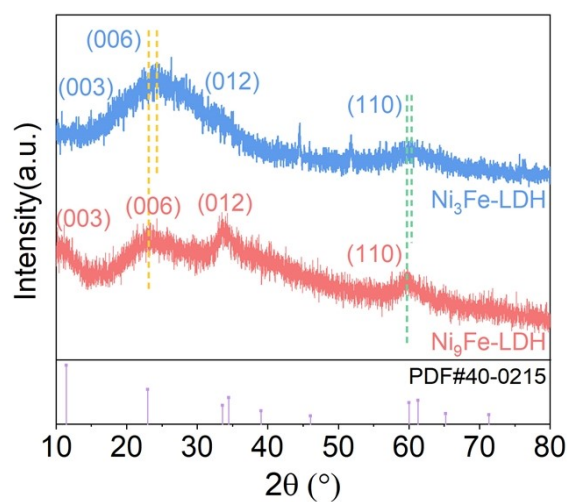
Fig. S1 XRD patterns of Ni$_3$Fe-LDH and Ni$_9$Fe-LDH.
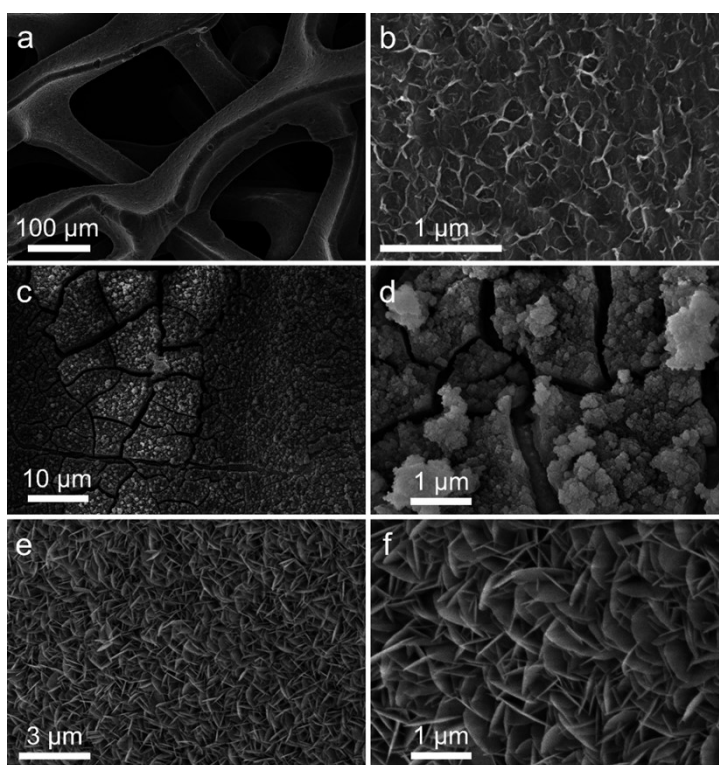
Fig. S2 SEM characterization of the Ni foam substrate, Ni$_3$Fe-LDH, and Ni(OH)$_2$. (a, b) Ni foam substrate at different magnifications, (c, d) Ni$_3$Fe-LDH at different magnifications, (e, f) Ni(OH)$_2$ at different magnifications.
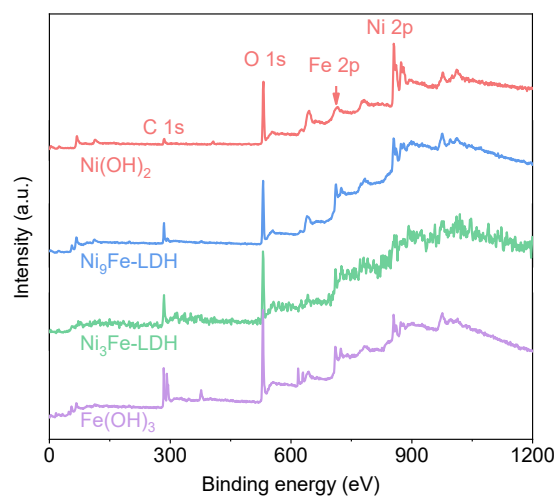
Fig. S3 XPS survey spectra of Ni(OH)$_2$, Ni$_9$Fe-LDH, Ni$_3$Fe-LDH, and Fe(OH)$_3$.
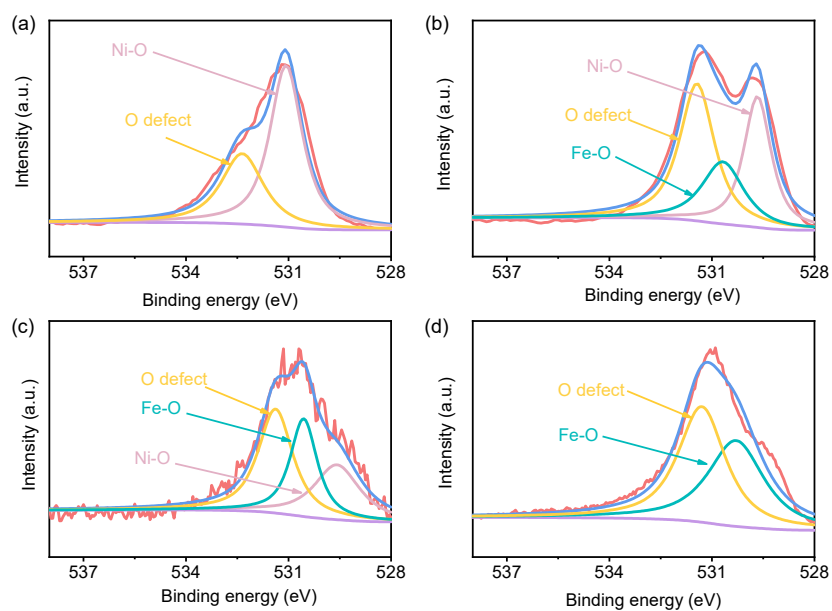
Fig. S4 High-resolution O 1s spectra of NiFe-LDH. (a) Ni(OH)$_2$, (b) Ni$_9$Fe-LDH, (c) Ni$_3$Fe-LDH, (d) Fe(OH)$_3$.

8
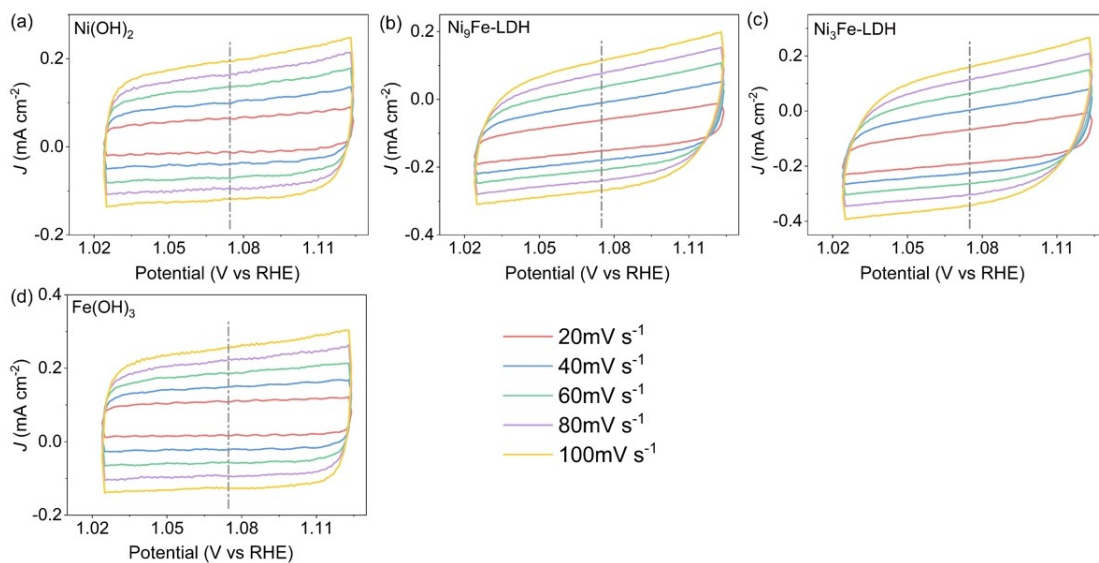
Fig. S5 CV curves of (a) $Ni(OH)_2$, (b) Ni_9Fe-LDH, (c) Ni_3Fe-LDH, and (d) $Fe(OH)_3$. The CV measurements were performed with various scan rates of 20, 40, 60, 80, and 100 mV s^{-1}.
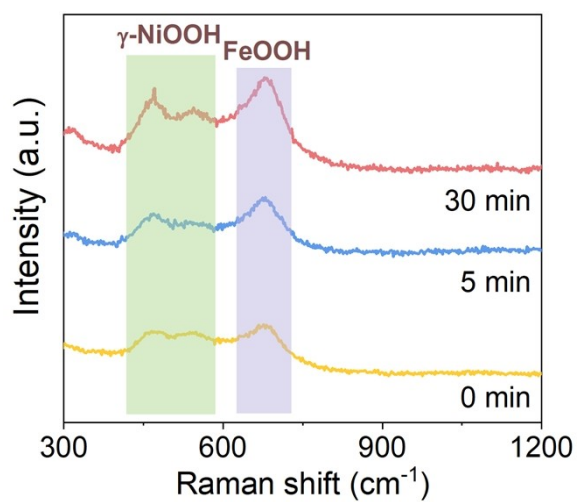
Fig. S6 Time-course Raman spectra of Ni_3Fe-LDH subsequent to different electrolysis durations at 10 mA cm^{-2}.
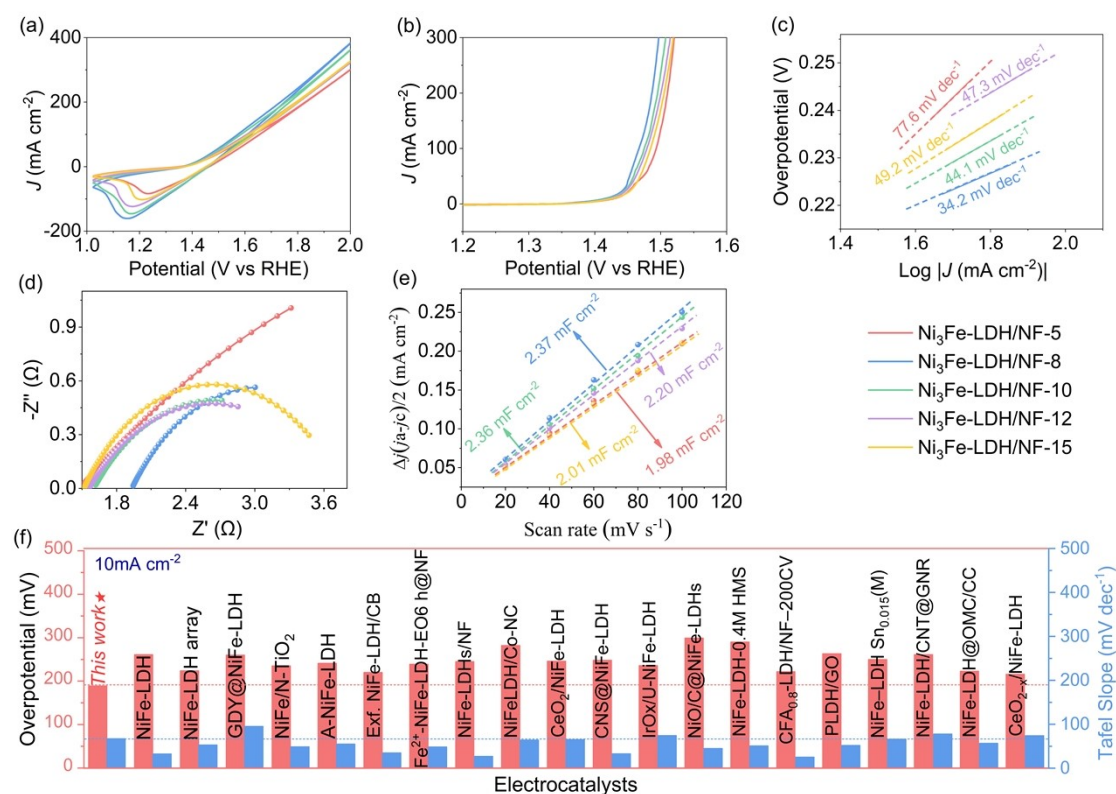
Fig. S7 Catalytic activity evaluation of Ni$_3$Fe-LDH/NF-t prepared under different deposition durations: 5, 8, 10, 12, and 15 min. (a) CV curves; (b) Polarization curves; (c) Tafel slopes deriving from corresponding polarization curves; (d) EIS spectra; (e) Electrochemical active surface area (ECSA); (f) Comparison of the overpotentials at 10 mA cm^{-2} and Tafel slopes with previously reported transition metal LDH-based electrocatalysts.

The optimization of the catalytic performance of Ni$_3$Fe-LDH was pursued by varying the electrodeposition durations, as shown in Fig. S7 and Table S4. The reduction peak of the Ni^{3+}/Ni^{2+} redox pair exhibits an initial increase followed by a decrease with extended electrodeposition durations (Fig. S7a). Notably, among all the samples, Ni$_3$Fe-LDH/NF-8 displays the broadest and most pronounced reduction peak, indicating a highly electron-rich local structure at the Ni sites. Evaluation of the polarization curves reveals that Ni$_3$Fe-LDH/NF-8 exhibits the highest OER activity,

10

requiring an impressively low overpotential of only 189 mV to achieve a current density of 10 mA cm^{-2} (Fig. S7b). This observation suggests that a moderate deposition time contributes to enhanced catalytic activity. Analysis of the Tafel plots (Fig. S7c) further demonstrates that Ni$_3$Fe-LDH/NF-8 exhibits the smallest Tafel slope (34.2 mV dec^{-1}) among all the samples (Ni$_3$Fe-LDH/NF-5, 77.6 mV dec^{-1}; Ni$_3$Fe-LDH/NF-10, 44.1 mV dec^{-1}; Ni$_3$Fe-LDH/NF-12, 47.3 mV dec^{-1}; Ni$_3$Fe-LDH/NF-15, 49.2 mV dec^{-1}), indicating its superior OER reaction kinetics. Additionally, Ni$_3$Fe-LDH/NF-8 shows the lowest charge transfer resistance (R_{ct}) of 1.90 Ω compared to the other samples (Ni$_3$Fe-LDH/NF-5, 2.60 Ω; Ni$_3$Fe-LDH/NF-10, 2.10 Ω; Ni$_3$Fe-LDH/NF-12, 2.13 Ω; Ni$_3$Fe-LDH/NF-15, 2.24 Ω) under an overpotential of 230 mV (Fig. S7d), thereby facilitating efficient electron transfer. The double-layer capacitance (C_{dl}) was derived from the CV curves measured at various scan rates (Fig. S8). As depicted in Fig. S7e, reveals that Ni$_3$Fe-LDH/NF-8 exhibits the largest C_{dl} value of 2.37 mF cm^{-2}, surpassing the other Ni$_3$Fe-LDH samples (Ni$_3$Fe-LDH/NF-5, 1.98 mF cm^{-2}; Ni$_3$Fe-LDH/NF-10, 2.36 mF cm^{-2}; Ni$_3$Fe-LDH/NF-12, 2.20 mF cm^{-2}; Ni$_3$Fe-LDH/NF-15, 2.01 mF cm^{-2}). This finding suggests that Ni$_3$Fe-LDH/NF-8 provides a greater number of active sites during the OER reaction process, further enhancing its catalytic performance. Notably, the as-prepared Ni$_3$Fe-LDH/NF-8 surpasses most of reported OER catalysts and locates among the most efficient ones (Fig. S7f and Table S5).
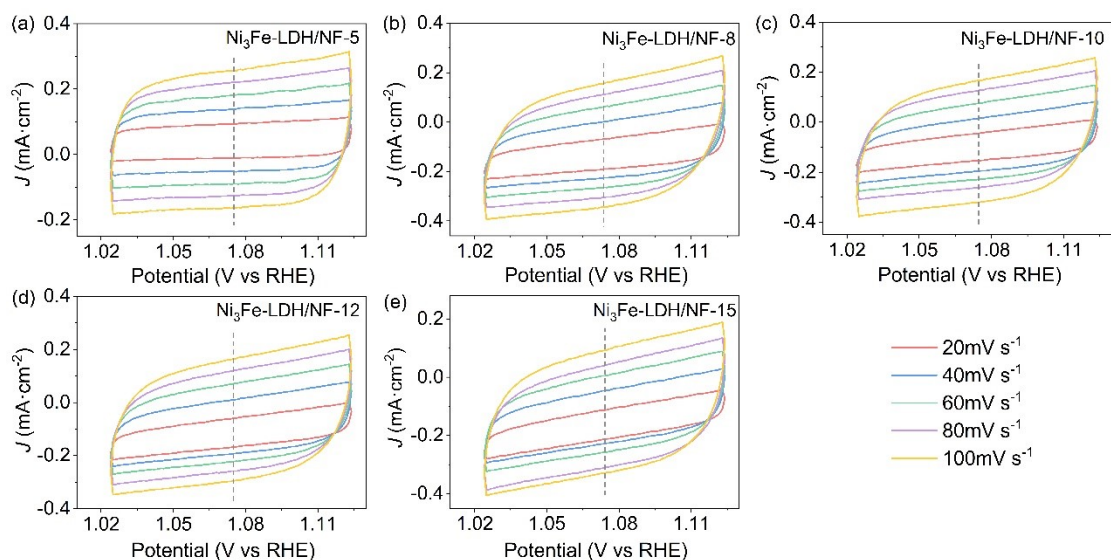
Fig. S8 CV curves measured with varying scan rates of 20, 40, 60, 80, and 100 mV s^{-1}. (a) Ni$_3$Fe-LDH/NF-5, (b) Ni$_3$Fe-LDH/NF-8, (c) Ni$_3$Fe-LDH/NF-10, (d) Ni$_3$Fe-LDH/ NF-12, (e) Ni$_3$Fe-LDH/NF-15.
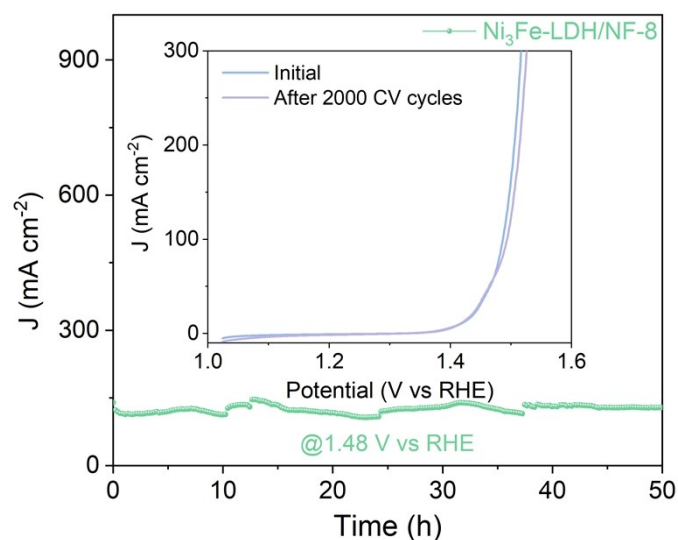
Fig. S9 Electrochemical stability evaluation of the Ni$_3$Fe-LDH/NF-8. 50-hour chronoamperometric test of Ni$_3$Fe-LDH/NF-8 at 1.48 V vs RHE. The inset is polarization curves of Ni$_3$Fe-LDH/NF-8 before and after 2000 cycles of CV test.

The stability of catalysts is a critical parameter in evaluating their practicality. To assess the OER stability of Ni$_3$Fe-LDH/NF-8, cyclic voltammetry (CV) scans were performed between 1.0 and 2.0 V vs. RHE at a scan rate of 100 mV s^{-1}, as shown in Fig. S9. Remarkably, even after undergoing 2000 consecutive cycles of measurement, no significant decay in activity is observed. The durability of Ni$_3$Fe-LDH/NF-8 is further confirmed by the stable current output during the chronoamperometry measurements over a 50-hour period. These findings highlight the excellent stability of Ni$_3$Fe-LDH/NF-8 as an OER catalyst, making it a promising candidate for practical applications.
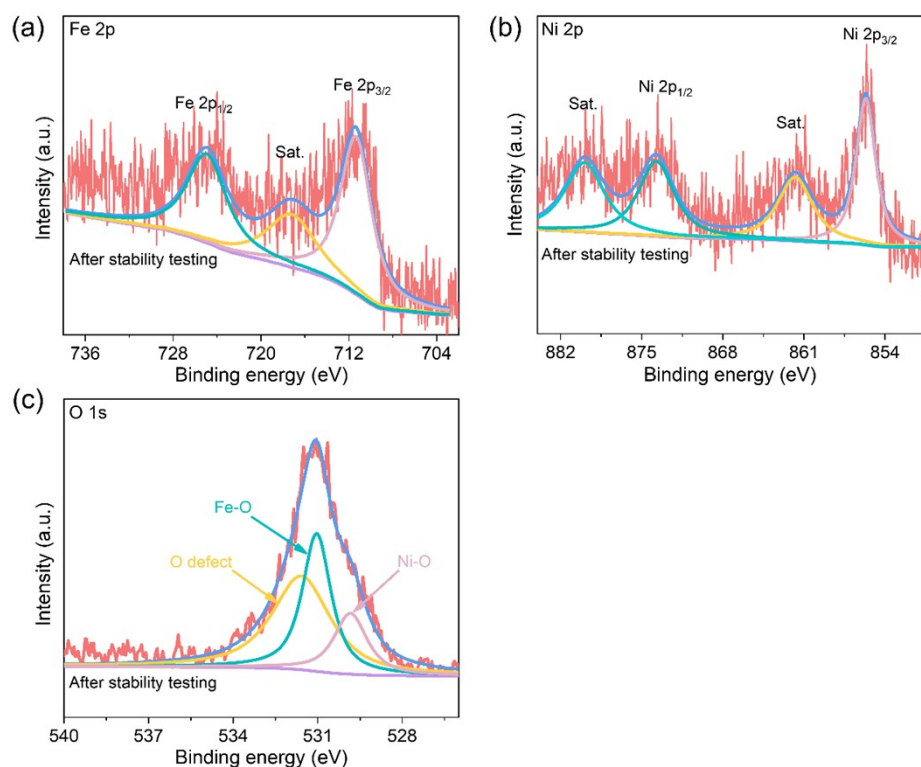
Fig. S10 XPS characterization of the post-reaction Ni$_3$Fe-LDH/NF-8. (a) Fe 2p spectra, (b) Ni 2p spectra, (c) O 1s spectra.
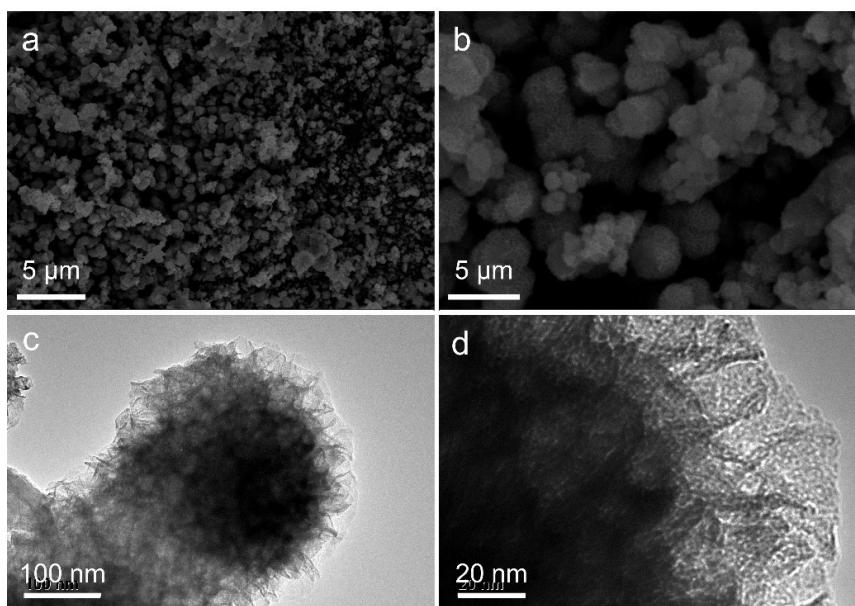
Fig. S11 SEM and TEM images of the post-reaction Ni$_3$Fe-LDH/NF-8. (a) and (b): SEM images, (c) and (d): TEM images.
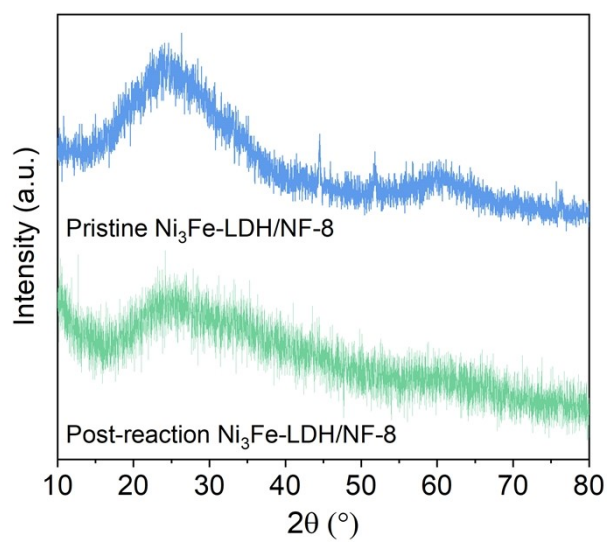
Fig. S12 XRD patterns of pristine and post-reaction Ni$_3$Fe-LDH NF-8.
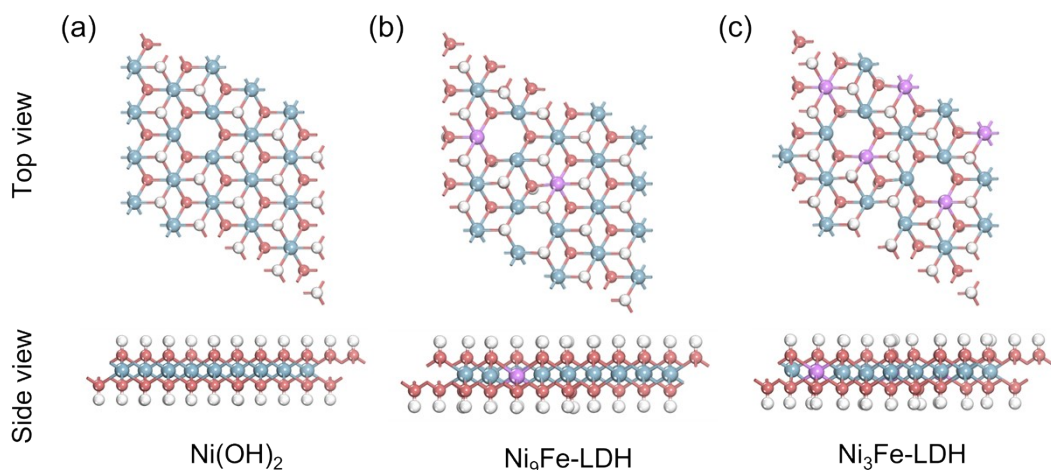
Fig. S13 Model structure constructed for DFT calculations. Top view and side view of the structures are separately shown on top and bottom. (a) $Ni(OH)_2$, (b) Ni_9Fe-LDH, (c) Ni_3Fe-LDH. In the model, $Ni(OH)_2$ removes 1 oxygen atom, Ni_9Fe-LDH removes 2 oxygen atoms, and Ni_3Fe-LDH removes 3 oxygen atoms, to simulate different oxygen vacancy concentrations. The blue, purple, pink, and white balls represent Ni, Fe, O, and H atoms, respectively.
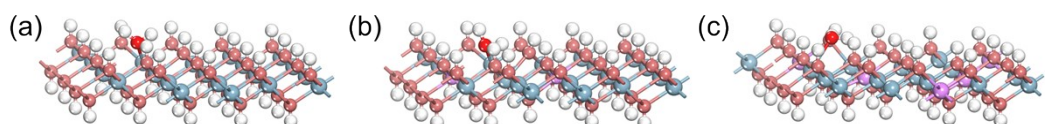
Fig. S14 Adsorption model of H_2O molecules. (a) $Ni(OH)_2$, (b) Ni_9Fe-LDH, and (c) Ni_3Fe-LDH.
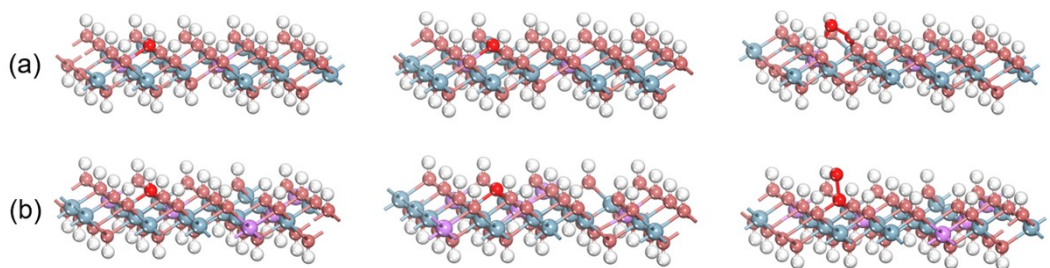
Fig. S15 Reaction coordinates adsorbed on (a) Ni$_9$Fe-LDH and (b) Ni$_3$Fe-LDH during OER reaction. Adsorptions of *OH, *O and *OOH on Ni active site are shown from left to right.
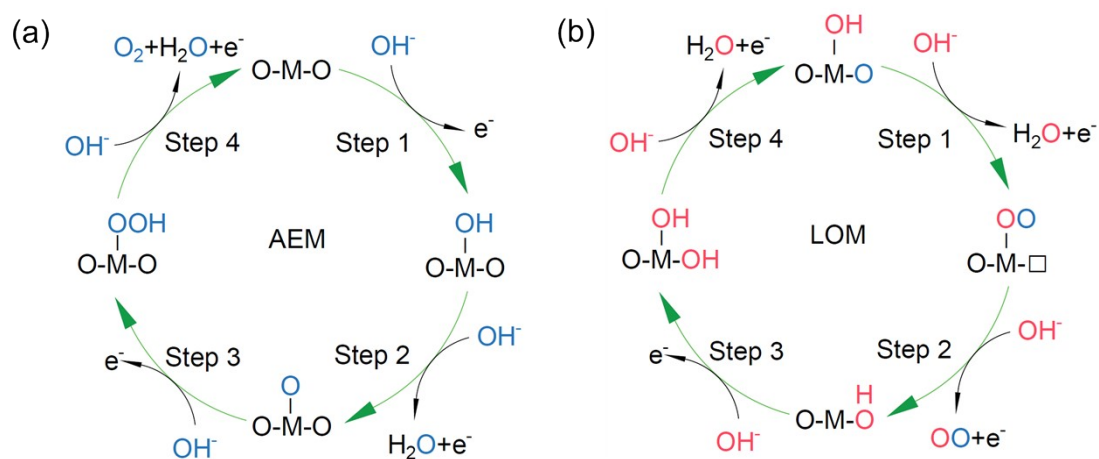
Fig. S16 Different reaction pathways for OER. (a) Adsorbate evolution mechanism (AEM). (b) Lattice oxygen oxidation mechanism (LOM).
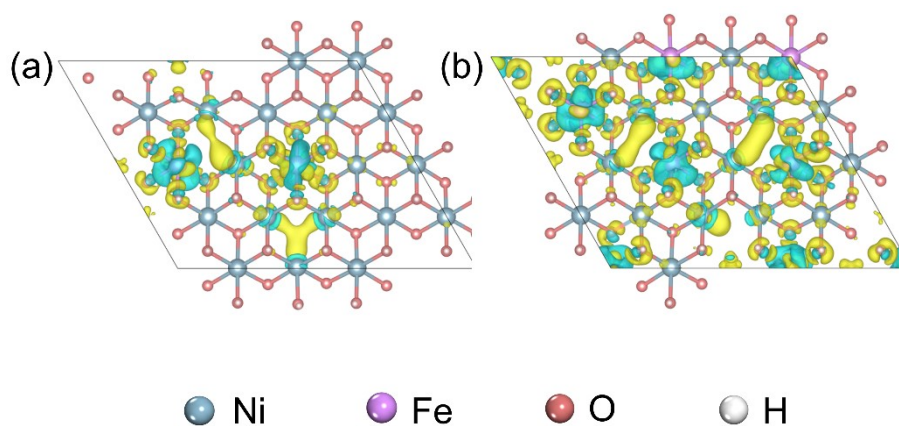
Fig. S17 Top view of the charge density differences. (a) Ni$_9$Fe-LDH, (b) Ni$_3$Fe-LDH.

3 Supplementary Tables

Table S1 Elemental composition of Ni_9Fe-LDH and Ni_3Fe-LDH detected by ICP-OES.

Samples	Elements	Content/g L^{-1}
Ni_9Fe-LDH	Ni	454.7
	Fe	51.1
Ni_3Fe-LDH	Ni	301.5
	Fe	102.7

Table S2 XPS (Ni 2p, Fe 2p and O1s regions) binding energy and assignment.

Sample	Binding energy/eV	Assignments
Ni(OH)$_2$	855.6	Ni 2p$_{3/2}$
	873.3	Ni 2p$_{1/2}$
	861.2	Satellite
	879.1	Satellite
	531.1	Ni-O, O 1s
	532.4	O$_V$, O 1s
Ni$_9$Fe-LDH	855.2	Ni 2p$_{3/2}$
	873.0	Ni 2p$_{1/2}$
	861.4	Satellite
	879.1	Satellite
	711.3	Fe 2p$_{3/2}$
	724.7	Fe 2p$_{1/2}$
	717.0	Satellite
	529.7	Ni-O, O 1s
	530.7	Fe-O, O 1s
	531.45	O$_V$, O 1s
Ni$_3$Fe-LDH	854.95	Ni 2p$_{3/2}$
	872.4	Ni 2p$_{1/2}$
	860.7	Satellite
	872.5	Satellite
	711.35	Fe 2p$_{3/2}$
	724.6	Fe 2p$_{1/2}$
	716.9	Satellite
	529.6	Ni-O, O 1s
	530.55	Fe-O, O 1s
	531.4	O$_V$, O 1s
Fe(OH)$_3$	711.25	Fe 2p$_{3/2}$
	724.5	Fe 2p$_{1/2}$
	716.1	Satellite
	530.3	Fe-O, O 1s
	531.3	O$_V$, O 1s

Table S3 Chemical bond length from the EXAFS spectra.

Sample	Type of band	R (Å)
Ni foil	Ni-Ni	2.17
NiO	Ni-O	1.65
	Ni-Ni	2.55
Ni_9Fe-LDH	Ni-O	1.20
	Ni-Ni/Fe	2.15
Ni_3Fe-LDH	Ni-O	1.59
	Ni-Ni/Fe	2.19

Table S4 Electrochemical results summarization of Ni_3Fe-LDH/NF-t during OER

processes

Sample	Overpotential @10 mA cm^{-2}	Tafel slope mV dec^{-1}	R_s/Ω	R_{ct}/Ω
Ni_3Fe-LDH/NF-5	199	77.6	1.45	2.60
Ni_3Fe-LDH/NF-8	189	34.2	1.59	1.90
Ni_3Fe-LDH/NF-10	195	44.1	1.60	2.10
Ni_3Fe-LDH/NF-12	197	47.3	1.56	2.13
Ni_3Fe-LDH/NF-15	199	49.2	1.52	2.24

Table S5 Comparison of Overpotential at 10 mA·cm^{-2} and Tafel slope of Ni$_3$Fe-LDH/NF-8 and currently reported LDH-based electrocatalysts.

Catalyst	Substrate	Overpotential @10 mA cm^{-2}	Tafel slope mV dec^{-1}	Ref
Ni$_3$Fe-LDH/NF-8	NF	189	67.2	This work
NiFe-LDH	GCE	261	32.5	5
NiFe-LDH array	NF	224	52.8	6
GDY@NiFe-LDH	Cu foil	260	95	7
NiFe/N-TiO$_2$	GCE	235	48.9	8
A-NiFe-LDH	GCE	241	55	9
Exf. NiFe-LDH/CB	GCE	220	35	10
Fe^{2+}-NiFe-LDH-EO6 h@NF	NF	239	48.3	11
NiFe-LDHs/NF	NF	245	27	12
NiFeLDH/Co-NC	GCE	282	64	13
CeO$_2$/NiFe-LDH	GCE	246	65	14
CNS@NiFe-LDH	CCF	248	32.9	15
IrOx/U-NiFe-LDH	NF	236	74.3	16
NiO/C@NiFe-LDHs	NF	299	45	17
NiFe-LDH-0.4M HMS	NF	290	51	18
CFA$_{0.8}$-LDH/NF–200CV	NF	222	25.4	19
PLDH/GO	NF	236	52	20
NiFe–LDH Sn$_{0.015}$(M)	NF	250	66	21
NiFe-LDH/CNT@GNR	NF	261	78	22
NiFe-LDH@OMC/CC	CC	223	56.6	23
CeO$_2$−x/NiFe-LDH	NF	216	74.1	24

Reference

1. G. Kresse and J. Furthmüller, *Phys. Rev. B*, 1996, **54**, 11169-11186.

2. G. Kresse and J. Furthmüller, *Comput. Mater. Sci.*, 1996, **6**, 15-50.

3. J. P. Perdew, K. Burke and M. Ernzerhof, *Phys. Rev. Lett.*, 1996, **77**, 3865-3868.

4. P. Zhai, M. Xia, Y. Wu, G. Zhang, J. Gao, B. Zhang, S. Cao, Y. Zhang, Z. Li, Z. Fan, C. Wang, X. Zhang, J. T. Miller, L. Sun and J. Hou, *Nat. Commun.*, 2021, **12**, 4587.

5. Y. Zheng, H. Deng, H. Feng, G. Luo, R. Tu and L. Zhang, *J. Colloid Interface Sci.*, 2023, **629**, 610-619.

6. Z. Li, M. Shao, H. An, Z. Wang, S. Xu, M. Wei, D. G. Evans and X. Duan, *Chem. Sci.*, 2015, **6**, 6624-6631.

7. G. Shi, C. Yu, Z. Fan, J. Li and M. Yuan, *ACS Appl. Mater. Interfaces*, 2019, **11**, 2662-2669.

8. X. Liu, Z. Chen and M. Cao, *ACS Appl. Energy Mater.*, 2019, **2**, 5960-5967.

9. J. Liu, J. Zhou, S. Liu, G. Chen, W. Wu, Y. li, P. Jin and C. Xu, *Electrochim. Acta*, 2020, **356**, 136827.

10. T. S. Munonde, H. Zheng and P. N. Nomngongo, *Ultrason. Sonochem.*, 2019, **59**, 104716.

11. Y. Wang, X. Zhang, L. Huang, Y. Guo, X. Yuan, H. Hou, J. Wu, C. Lu and Y. Zhang, *J. Colloid Interface Sci.*, 2021, **599**, 168-177.

12. R. A. Senthil, J. Pan, X. Yang and Y. Sun, *Int. J. Hydrogen Energy*, 2018, **43**, 21824-21834.

13. S. Zhu, J. Wang, H. Li, J. Cai, Y. Li, J. Hu, Y. He and Y. Zhou, *ACS Appl. Nano Mater.*, 2022, **5**, 13047-13054.

14. Q. Dong, C. Shuai, Z. Mo, N. Liu, G. Liu, J. Wang, H. Pei, Q. Jia, W. Liu and X. Guo, *J. Solid State Chem.*, 2021, **296**, 121967.

15. Y. Kong, J. Li, Y. Wang, W. Chu and Z. Liu, *Catal. Lett.*, 2020, **150**, 3049-3057.

16. D. Liu, Y. Du, T. Li, H. Zhang, D. Liu, W. Zhang, H. Tang, Y. Hou, J. Li, S. Yan, T. Yu and Z. Zou, *Chem. Commun.*, 2020, **56**, 11465-11468.

17. X. Li, M. Fan, D. Wei, X. Wang and Y. Wang, *J. Electrochem. Soc.*, 2020, **167**, 024501.

18. H. Zhong, T. Liu, S. Zhang, D. Li, P. Tang, N. Alonso-Vante and Y. Feng, *J. Energy Chem.*, 2019, **33**, 130-137.

19. J. Zhong, Q. Chen, C. Guo, W. Peng, Y. Li, F. Zhang and X. Fan, *Int. J. Hydrogen Energy*, 2023, **48**, 23530-23539.

20. J. Xie, C. Li, J. Niu, S. Zhang, X. Ou, P. Feng and H. Garcia, *Mater. Lett.*, 2021, **290**, 129517.

21. K. Bera, R. Madhu, H. N. Dhandapani, S. Nagappan, A. De and S. Kundu, *Inorg. Chem.*, 2022, **61**, 16895-16904.

22. X. Yin, Y. Hua, W. Hao, J. Yang and Z. Gao, *Electrochim. Acta*, 2022, **420**, 140455.

23. G. Huang, C. Zhang, Z. Liu, S. Yuan, G. Yang and N. Li, *Appl. Surface Sci.*, 2021, **565**, 150533.

24. Y. Du, D. Liu, T. Li, Y. Yan, Y. Liang, S. Yan and Z. Zou, *Appl. Catal. B-*

Environ., 2022, **306**, 121146.